Computational modeling of tensile split-Hopkinson bar tests on carbon-carbon composites using continuum and mesoscale approaches

Christopher Sorini[1], Roberto Enriquez Vargas[1], Alexander Carpenter[1], Drew Hackney[1], Sidney Chocron[1]

[1]Computational Mechanics Section, Engineering Dynamics Department, Mechanical Engineering Division, Southwest Research Institute (SwRI), San Antonio, TX, USA

1 Abstract

The high strength, toughness, quasi-ductility over monolithic ceramics, and elevated temperature oxidation resistance make carbon-carbon (C/C) ceramic matrix composites (CMCs) excellent candidates for hypersonic vehicle components, which will experience high temperatures and oftentimes high strain rates in service. However, accurate characterization of the material behavior under such extreme/harsh conditions presents significant challenges.

This work describes the results of LS-DYNA computations conducted in support of an ongoing Southwest Research Institute (SwRI) internal research (IR) program focused on the high temperature, high strain rate behavior of C/C composites. The goal of this IR program is to develop and fabricate a system capable of rapidly heating metals and C/C CMC test specimens up to 4000°F to facilitate elevated temperature tensile split-Hopkinson pressure bar (SHPB) testing. The focus of this paper is the use of explicit finite element (FE) simulations to support the experimental program.

Results of a computational investigation into apparent non-equilibrium behavior exhibited in previous SHPB tension tests conducted on a commercial off the shelf (COTS) C/C composite material are presented. Said non-equilibrium behavior is suggested by the dissimilarity of the forces on the ends of the specimen (computed from the transmitted wave and the sum of the incident and reflected waves measured in the tests). In the computations, the entire SHPB set up is represented/meshed. Two different approaches are taken to model the SHPB tension test coupons. The first approach considers the woven C/C CMC as a smeared homogeneous continuum. These continuum simulations result in sudden, brittle failure of the specimen, which leads to attenuation of the transmitted strain signals (i.e., the transmitter bar strain signals decrease in amplitude with increasing propagation distance). To correlate the simulated and experimental strain amplitude at the location of the transmitter bar strain gage in the tests, it was found that the value of the maximum principal stress at failure in the continuum models needed to be increased to what the authors believe is an unrealistically large value. It was also found that the continuum modeling approach is unable to capture the widening of the transmitter bar signals that is present in the SPHB experimental data. In the second modeling approach, the woven C/C CMC mesostructure (i.e., the tows and matrix) are explicitly modeled. Compared to the continuum simulations, the mesoscale simulations exhibited a more progressive failure, which better matched the test data and was found to result in enough additional “ductility” such that the amplitude of the strain and force signals did not decrease with increasing propagation distance along the transmitter bar. Whereas the maximum principal stress at failure used in the continuum models had to be unrealistically increased to correlate the simulated transmitted strain signals to those in the experiment, this was not the case for the failure properties used for the tows and matrix in the mesoscale simulations. The simulated transmitted waves in the mesoscale simulations were wider than those in the continuum simulations and were in good agreement with those in the experiments in terms of the overall shape and amplitude. Simulated section forces on the incident and transmitter bar sides of the specimen gage section indicate the specimen achieves stress equilibrium during the test despite the non-equilibrium suggested by the test data.

2 Tensile SHPB Tests

2.1 Materials and Test Methods

The material used in this work is a COTS 12K woven C/C CMC produced by CeraMaterials under the trade name CM-147-12 [1]. The bulk density is 1.47 g/cm^3. We estimate the porosity is between 15%

and 20%. GraphiMaterials, a subsidiary of CeraMaterials, states a typical fiber volume fraction of 60% [2], but does not specify the material grade, so it is unknown whether this applies to CM-147-12. We believe the fiber volume fraction is likely somewhere between 50% [3] and 60%. Though not stated explicitly by the manufacturer, it was determined via inspection that the composite architecture is a 2x2 twill weave. All tested specimens were cut from a nominally 0.25 inch thick C/C panel with approximately ten layers of the braided preform through the thickness. While various modifications of the specimen geometry have been made throughout the ongoing research program, the geometry that is simulated in this manuscript is shown in Fig.1, where all dimensions are in inches.

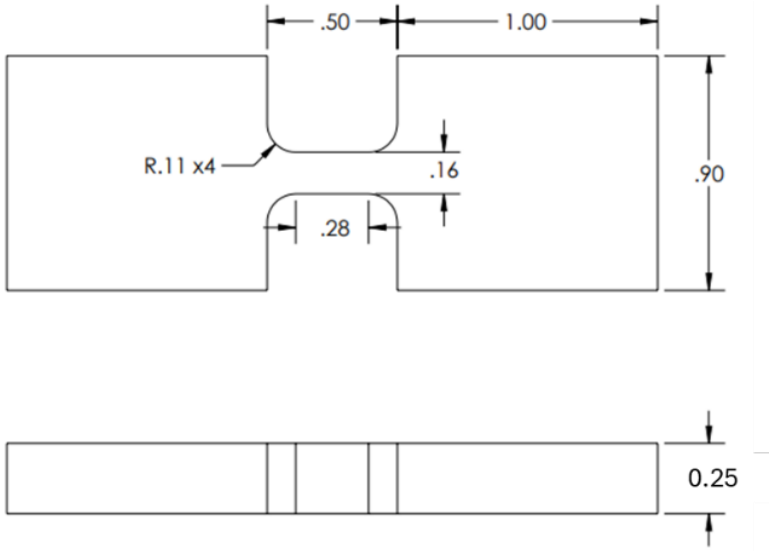

Fig.1: Specimen geometry used for high rate tension testing. All dimensions are in inches.

High strain rate tests were performed at SwRI using a tensile SHPB [4, 5, 6] consisting of a 1” diameter solid maraging steel incident bar and an aluminum tube as the transmitter bar. The hollow transmitter bar had inner and outer diameters of 0.875” and 1”, respectively. The aluminum tube was used to increase the bars sensitivity to the force transmitted through the specimen into the transmitter bar. Traditional foil strain gauges were used for the steel incident bar whereas the hollow aluminum transmitter bar was instrumented with semiconductor strain gauges. All tests used a 24” long maraging steel striker bar to generate the incident wave.

Epoxy was used to bond the specimens to the faces of the grips, which were comprised as the same materials as the bars (steel on incident bar side and aluminum on transmitter bar side). No pulse shaper was used for the tests described in this manuscript unless stated otherwise. The tensile SHPB bar in the SwRI Engineering Dynamics Department [7, 8] used for the testing is shown in Fig.2.

Fig.2: Tensile SHPB in the SwRI Engineering Dynamics Department.

2.2 High-Rate Tension Test Results

The results presented in this section are from room temperature tensile SHPB tests conducted in May 2023. It is noted that for elevated temperature tests (not presented in this manuscript), the specimen geometry has four tabs on the grip section that extend outward in the width direction to facilitate the connections required to apply the electric current to rapidly heat the specimen. Three tests were conducted, each of which had striker bar impact velocities of around 300 in/sec (7.62 m/s). The raw strain wave signals recorded on the incident and transmitter bars gages in one of these tests is shown in Fig.3.

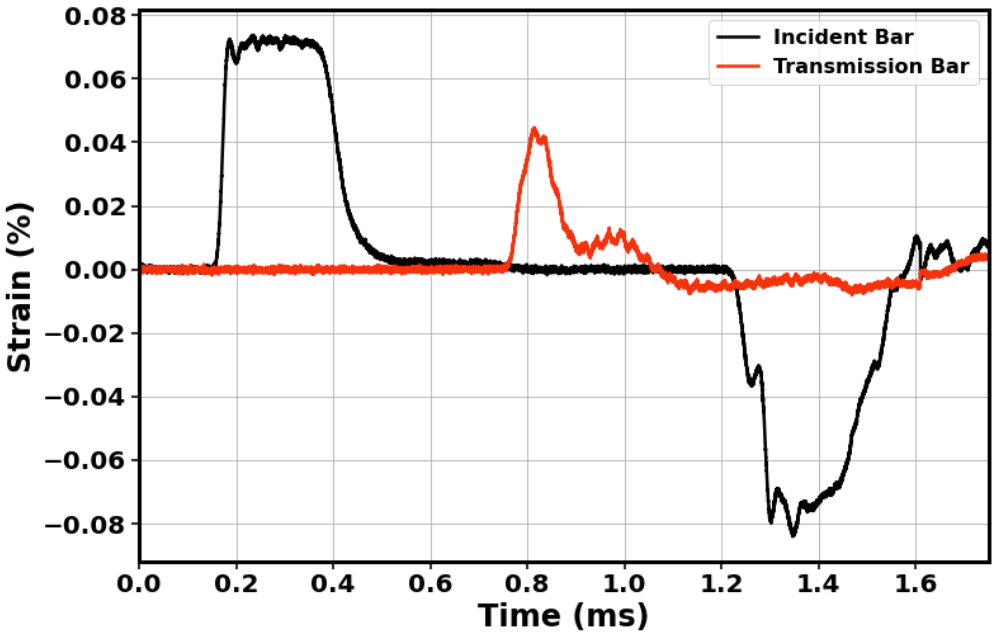

Fig.3: Raw strain signals measured at incident and transmitter bar strain gages in a tensile SHPB test.

One of the requirements of a valid SHPB test is specimen equilibrium, which is typically verified by computing the forces on either side of the specimen from the incident, reflected, and transmitted strains

measured at the bar strain gages [9]. The time history of the force at the incident bar-specimen interface, F_{IR}, is computed from the (time-shifted) sum of the incident and reflected wave strain signals (ε_I and ε_R) as well as the incident bar cross sectional area (A_I) and elastic modulus (E_I) using Equation 1. Similarly, the time history of the force at the transmitter bar-specimen interface, F_T is computed from the transmitted wave strain signal (ε_T) as well the transmitter bar cross sectional area (A_T) and modulus (E_T) using Equation 2.

$$F_{IR} = E_I A_I (\varepsilon_I + \varepsilon_R) \tag{1}$$

$$F_T = E_T A_T \varepsilon_T \tag{2}$$

The forces at each of the bar-specimen interfaces should be similar for the specimen to have been in equilibrium during the tests. Plots of the time history of forces at the bar-specimen interfaces computed using Equations 1 and 2 are shown in Fig.4.

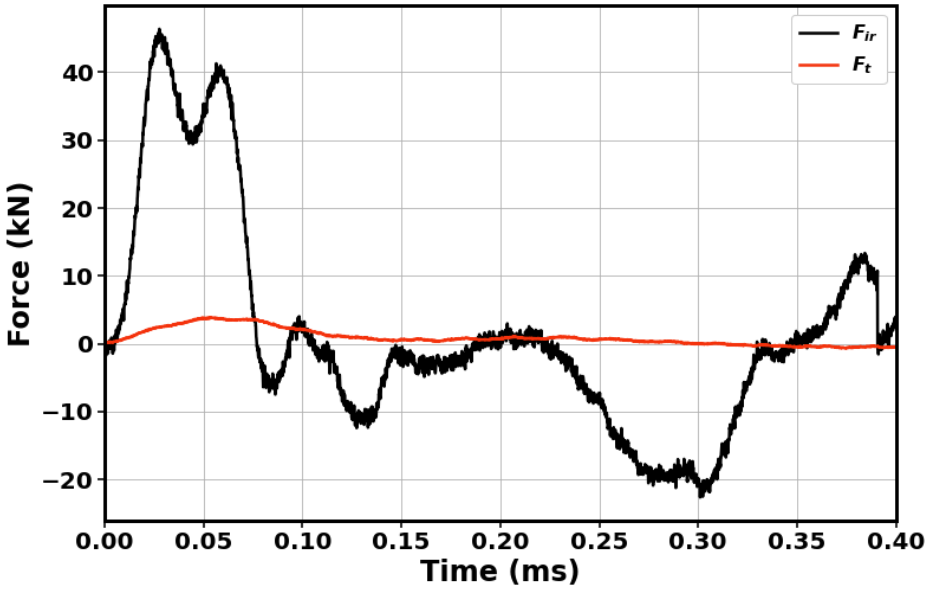

a)

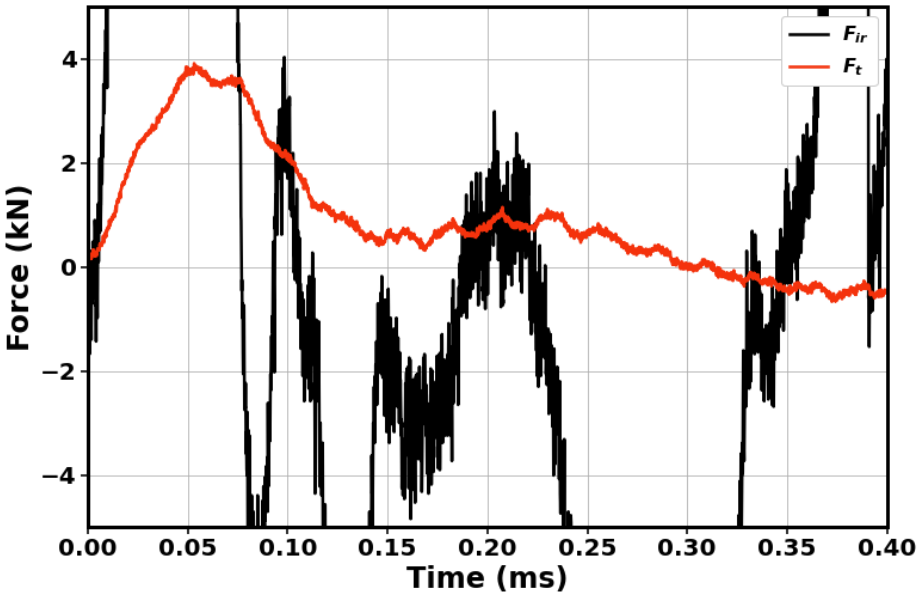

b)

Fig.4: a) Forces on the incident and transmitter bar-specimen interfaces for a tensile SHPB test computed using Equations 1 and 2; b) Close-up of force on transmitter bar-specimen interface.

The results in Fig.4 clearly show there is a large disparity in the bar-specimen interface forces computed from the strain gage measurements. The estimated force on the incident bar-specimen interface is roughly an order of magnitude larger than that on the transmitter bar-specimen interface for all three tests. Additionally, the transmitted wave signals are significantly wider than those of the incident wave.

These results suggest that either the specimen did not achieve equilibrium in these tests or that the forces computed using the strain gage signals are not representative of the forces experienced by the specimen at the bar-specimen interfaces. It is noted that the test specimen failed in the gage section in all three of these tests, so the tests were valid in this regard. Results of a computational investigation into reasons for this apparent nonequilibrium behavior are presented in the next section.

3 Tensile SHPB Simulations

LS-DYNA simulations were conducted to computationally reproduce the test results described in the previous section (Fig.3 and Fig.4). The goal of these simulations is to gain insight into reasons for the apparent non-equilibrium suggested by the test data and to assess the validity of the tests.

To investigate the effects of the epoxy used to bond the specimen to the grips on the measured results, simulations of the SHPB tests were conducted both with and without epoxy using a homogeneous mesh of the specimen. In the computations, the entire SHPB set up is represented/meshed. Fig.5 shows images of the homogeneous specimen mesh in the grips, both with (middle) and without epoxy (bottom), as well as an image of the SHPB mesh (top). The epoxy in the mesh is 0.5 mm thick and was modeled as linear elastic and isotropic using ***MAT_ELASTIC** with a Young's modulus of 1.11 GPa and Poisson's ratio of 0.34. The choice was made to use one solid element through the thickness of the epoxy to maintain a reasonable stable timestep in the simulations. Failure of the epoxy has not been considered; we are interested here in how the compliance of the epoxy affects the measured response of the specimen. An orthotropic elastic material constitutive model (***MAT_ORTHOTROPIC_ELASTIC**) with a maximum principal stress failure criterion (specified via a ***MAT_ADD_EROSION** card) was utilized for the homogeneous dogbone specimen mesh. The in-plane elastic moduli of the specimen were set to 50 GPa based on previous quasi-static tensile tests. All the parts in the SHPB mesh (Fig.5, top) were represented with reduced integration solid elements (**ELFORM**=1 on the ***SECTION_SOLID** card).

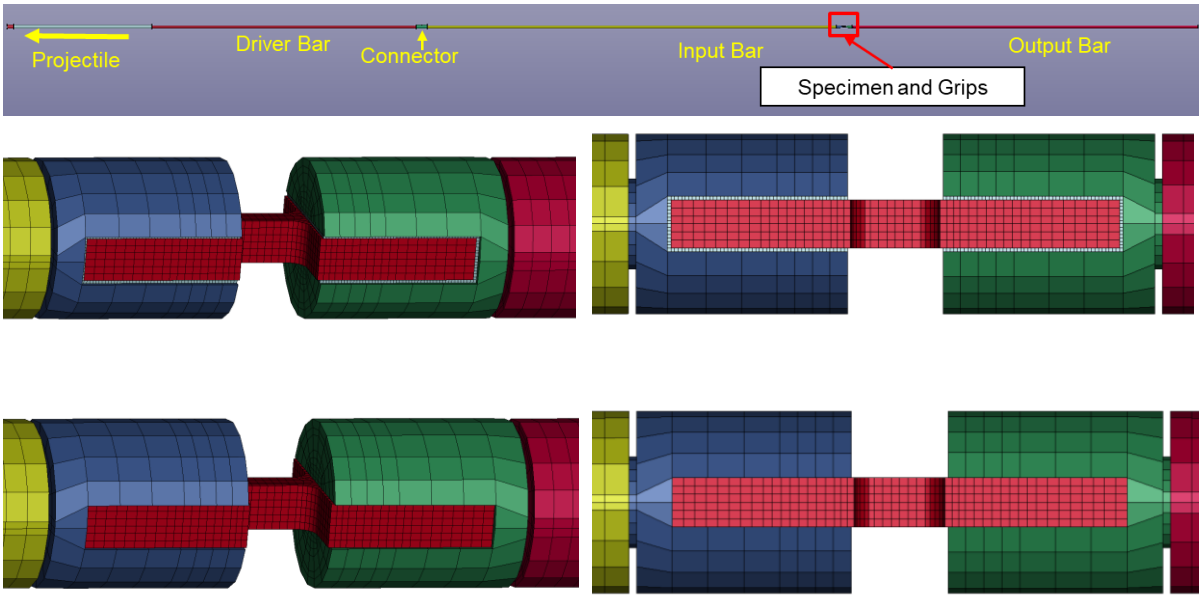

Fig.5: Tensile SHPB mesh (top); Close-up view of of grips and homogeneous dogbone specimen meshes with (middle row) and without (bottom row) epoxy. The grip mesh shown in blue is on the the incident bar side and that shown in green is on the transmitter bar side.

Fig.6 shows SHPB simulation results of strain at an element at the location of the strain gage on the transmitter bar in the tests for cases with and without epoxy. These simulations utilized the homogeneous dogbone geometry mesh shown in Fig.5. The maximum principal stress at failure used for **SIGP1** on the ***MAT_ADD_EROSION** card for the specimen in these simulations was 120 MPa.

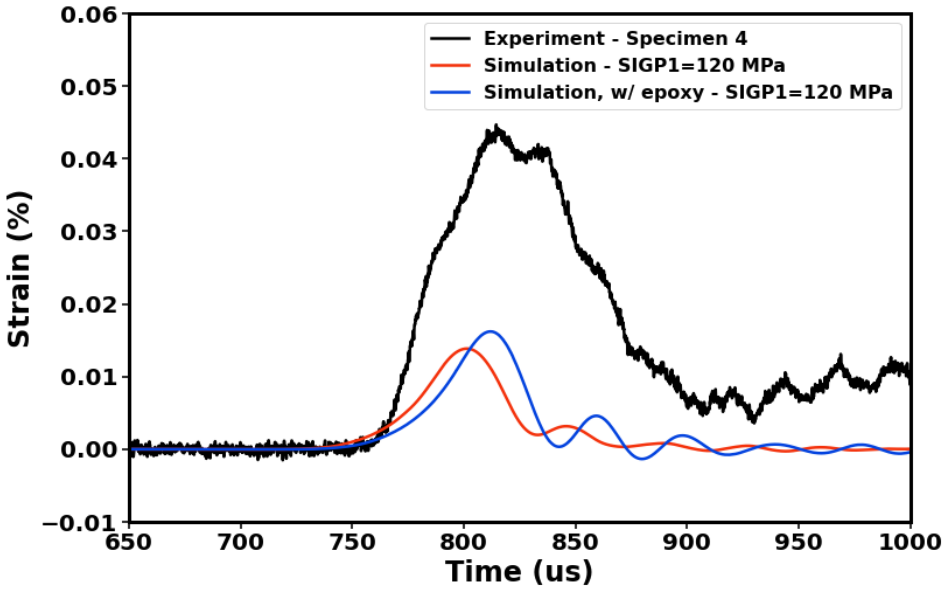

Fig.6: Simulated vs. experimental strain signals at transmitter bar strain gage in homogeneous dogbone SHPB simulations with effective principal stress at failure (SIGP1) of 120 MPa.

It is evident in Fig.6 that the presence of the epoxy slightly increases the peak strain at the transmitter bar strain gage in the simulation, but it does not result in an appreciably wider signal compared to the case with no epoxy. Fig.7 shows simulated transmitter bar strain gage signals at the location of the strain gage in the test as well as two other locations further down the bar for the simulation cases shown in Fig.6. The results in Fig.7 show that the signal is being slightly attenuated/dispersed as it propagates along the bar for the cases with and without epoxy.

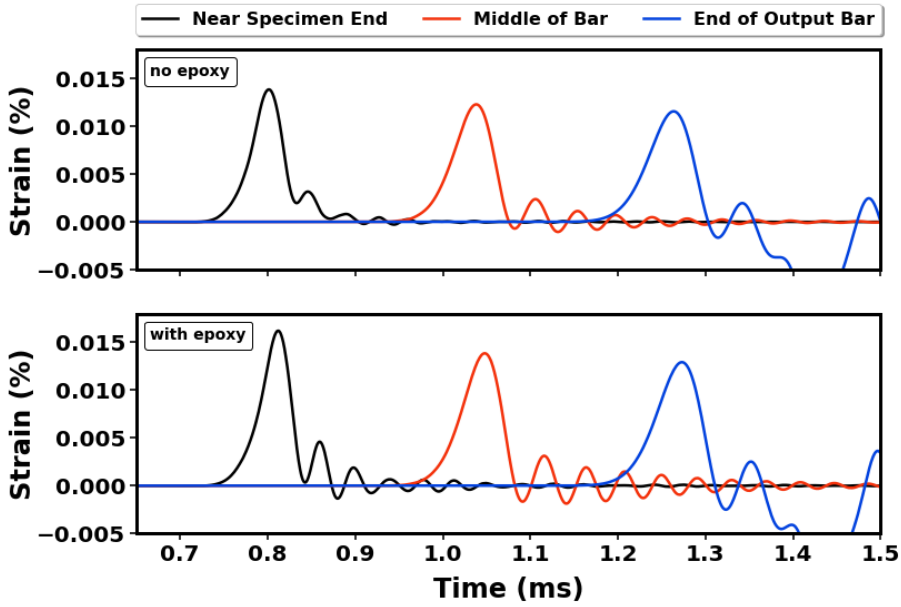

Fig.7: Simulated strain gage signals at various locations along the length of the transmitter bar for homogeneous mesh cases with and without epoxy with effective principal stress at failure (SIGP1) of 120 MPa.

Given that the simulated amplitude of the strain signal at the location of the transmitted bar strain gage is significantly lower than that measured in the experiment (Fig.6), simulations were performed to determine the maximum principal stress at failure required in the simulations to result in a simulated transmitted bar strain signal that is of equal amplitude to that in the experiment. Through these simulations, it was determined that maximum principal stress at failure values of 280 MPa and 320 MPa were required in the cases with and without epoxy, respectively, to correlate the simulated & experimental transmitter bar strain gage signal amplitudes. Fig.8 shows these simulated strain gage signals.

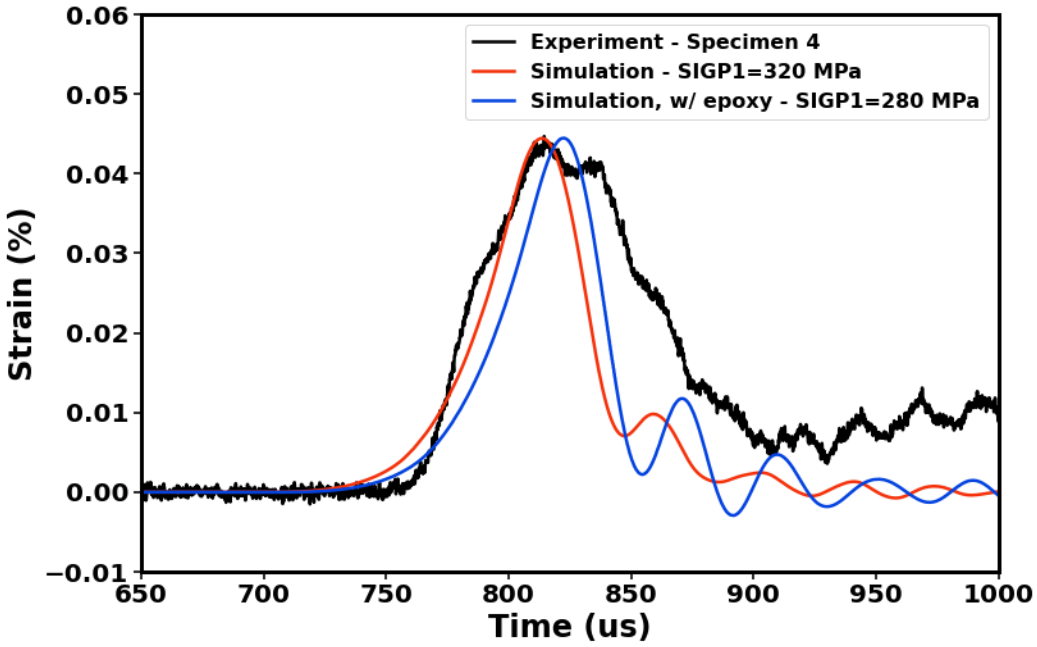

Fig.8: Simulated vs. experimental strain signals at transmitter bar strain gage in homogeneous specimen SHPB simulations after adjusting effective principal stress at failure (SIGP1) to correlate with experiment.

Fig.9 shows the simulated transmitter bar strain gage signals at the location of the strain gage in the test as well as two other locations further down the bar for the cases with and without epoxy shown in Fig.8. It is evident in Fig.9 that the strain amplitude decreases with increasing propagation distance along the transmitter bar.

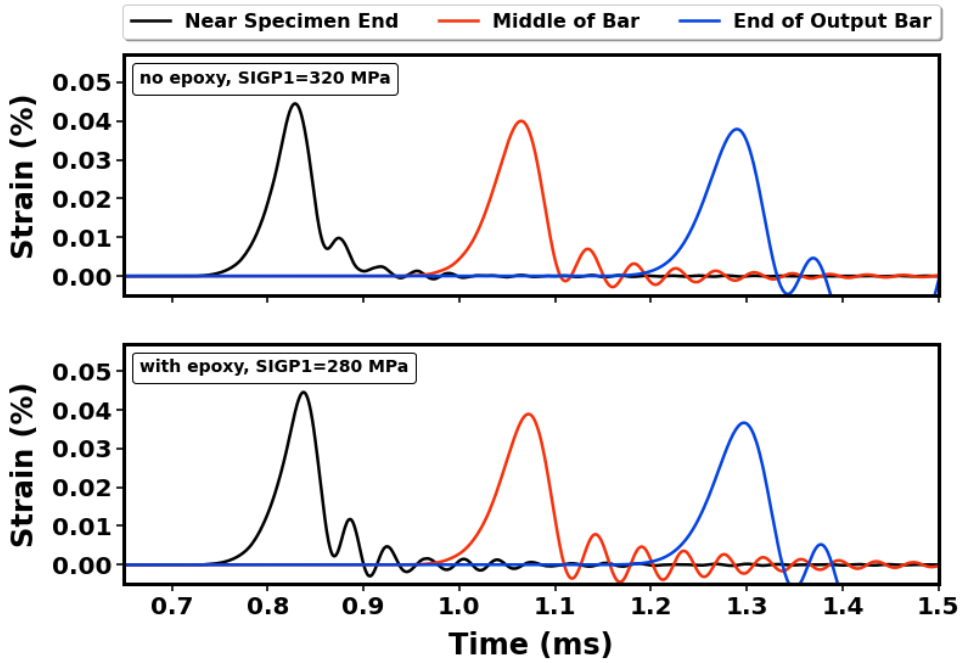

Fig.9: Simulated strain gage signals at various locations along the length of the transmitter bar for homogeneous mesh cases with and without epoxy with effective principal stress at failure (SIGP1) of 320 MPa (no epoxy) and 280 MPa (with epoxy).

Given that the homogeneous dogbone specimen simulations with epoxy did not show any widening of the transmitter bar strain gage signal and all (both with and without epoxy) exhibited a decrease in the transmitted strain signal amplitude with increasing propagation distance, we suspected that dispersion could be greatly affecting the wave propagation, i.e., the wave in the transmitter bar does not represent the specimen behavior. To further investigate this, a mesoscale mesh of the dogbone specimen that explicitly models the carbon-carbon composite tows and matrix was developed. The goal is to determine if explicitly modeling the mesostructure will result in enough additional "ductility" in the simulated specimen to prevent significant attenuation/dispersion of the strain signal with increasing propagation distance down the transmitter bar. Additionally, the mesoscale simulations may help explain the widening of the transmitter bar signals seen in the test data, which was not captured by the simulations with the homogeneous mesh, which all exhibited a sudden, brittle failure.

Fig.10 shows the mesoscale mesh of the dogbone specimen, where the bright red box denotes an individual repeating unit cell (RUC) of the 2x2 twill weave architecture. In the meshes of the mesoscale specimen and RUC, red elements represent matrix material whereas the blue and green elements represent the 12K tows. The in-plane dimensions of the RUC mesh are approximately the same as those of the actual material (roughly 1 cm by 1 cm). The specimen mesh consists of ten RUCs through the thickness. Prior to generating the specimen mesh, matrix material elements were removed at random from the RUC mesh to achieve an overall void volume fraction of approximately 16%. The tow and matrix volume fractions of the RUC mesh are 66% and 18%. These volume fractions are roughly the same in the mesoscale specimen mesh as it was constructed by assembling multiple RUCs. An orthotropic material model was used to describe the constitutive behavior of the tows whereas the matrix was modeled as isotropic. An equivalent (i.e., von Mises) stress failure criterion was employed for both the tows and matrix. Note that this isotropic failure criterion is technically not appropriate for the tows due to their orthotropy. As such, a different failure criterion for the tows may be used in the future. For the mesoscale simulations, fully integrated solid elements (**ELFORM**=2 on the ***SECTION_SOLID** card) were used for the tows and reduced integration solids were used for all the other parts. It is noted that only cases with epoxy have been considered for the mesoscale simulations.

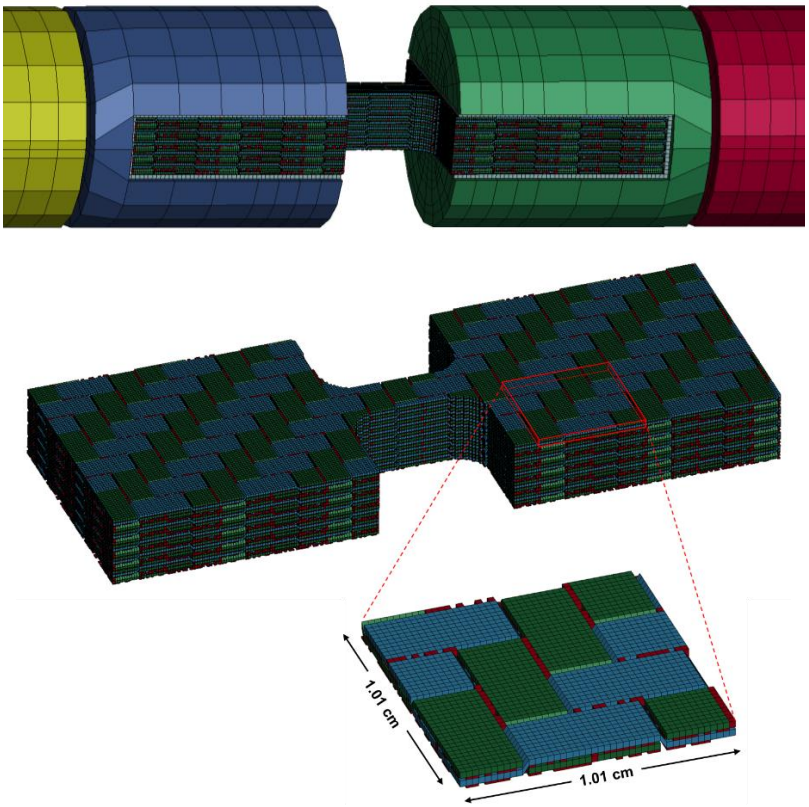

Fig.10: Dogbone specimen mesoscale mesh.

Fig.11 shows simulated and experimental strain signals at the transmitter bar strain gage in mesoscale dogbone SHPB simulations for various cases. The effective stress at failure values used for the simulations labeled as “IR_HC_0002”, “IR_HC_0004”, and “IR_HC_0005” in the legend of Fig.11 are shown in Table 1.

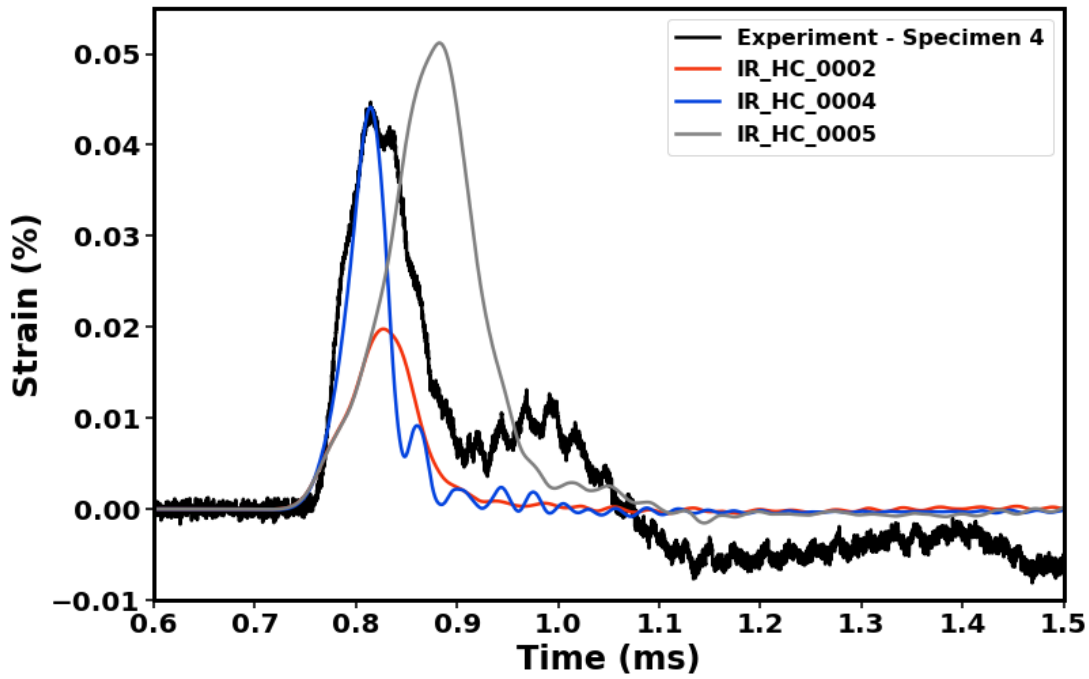

Fig.11: Simulated vs. experimental strain signals at transmitter bar strain gage in mesoscale dogbone SHPB simulations.

Simulation	Effective Stress at Failure (MPa)	
	Tow	Matrix
IR_HC_0002	2600	20
IR_HC_0004	2600	200
IR_HC_0005	5670	20

Table 1: Effective stress at failure for the tows and matrix in the mesoscale SHPB simulations.

In Fig.11, the simulation denoted “IR_HC_0004” correlates well with the magnitude of the experimental transmitter bar strain gage signal. However, the failure effective stress value for the matrix is likely unrealistically high. Additionally, while “IR_HC_0004” correlates with the peak strain signal, it fails to capture the shape/structure of the experimental strain signal. The only difference between the inputs in simulations “IR_HC_0002” and “IR_HC_0004” is that the failure effective stress of the matrix is ten times greater in “IR_HC_0004”. The difference in the simulated amplitude and slope of the strain signal in simulations “IR_HC_0002” and “IR_HC_0004” is therefore solely due to the difference in the failure effective stress value of the matrix despite this value being nominal compared to that of the tows in both cases. Fig.11 also indicates both simulation cases with a matrix effective failure stress of 20 MPa (“IR_HC_0002” and “IR_HC_0005”) result in a wider signal compared to simulation “IR_HC_0004” and the simulations that employed the homogeneous specimen mesh.

Fig.12 shows the forces at cross sections on the mesoscale specimen mesh for simulations “IR_HC_0004” and “IR_HC_0005”. The coincidence of the forces at the simulated specimen ends for each of the two cases shown indicates the specimens are in equilibrium. However, it is evident that the “IR_HC_0004” specimen fails in a brittle manner whereas “IR_HC_0005” exhibits a more progressive failure. It is noted that, while not shown, all the simulations that employed the homogeneous dogbone specimen mesh failed in a brittle manner similar to mesoscale simulation "IR_HC_0004".

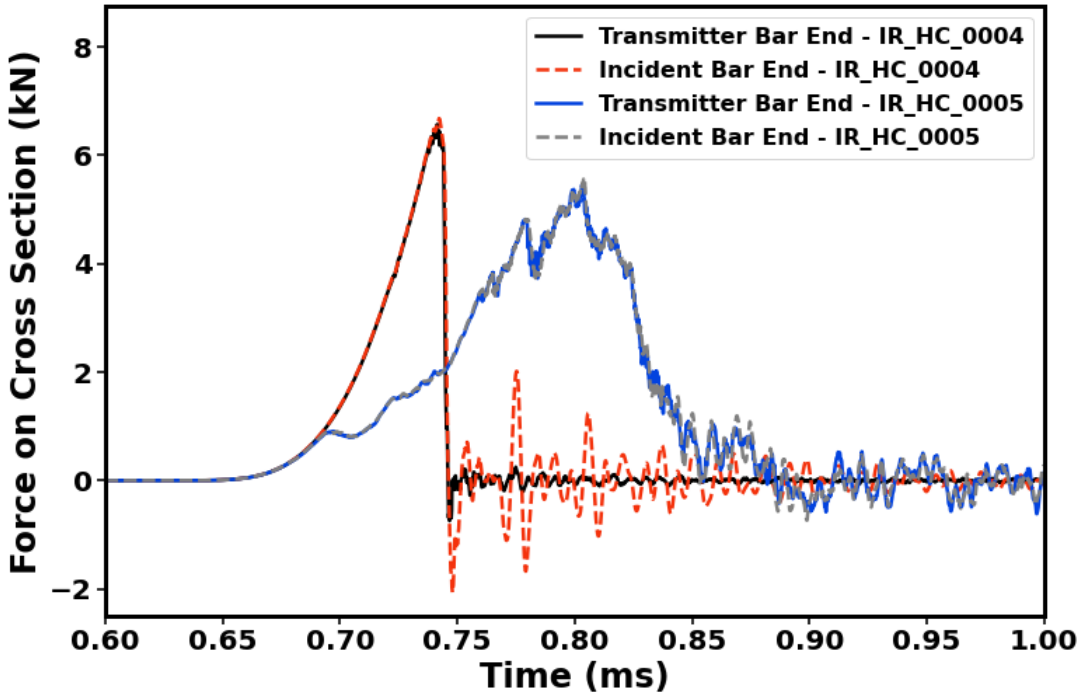

Fig.12: The simulated forces at each end of the gage section of the mesoscale dogbone specimen mesh are compared during the SHPB simulation.

Fig.13 shows simulated strain gage signals at various locations along the length of the transmitter bar for mesoscale simulations “IR_HC_0002”, “IR_HC_0004”, and “IR_HC_0005”. The homogeneous mesh case with epoxy and a maximum principal failure stress of 280 MPa is also shown for comparison.

Similar to the homogeneous mesh simulations shown earlier in this section, the amplitude of the strain in mesoscale simulation “IR_HC_0004” decreases as it propagates down the transmitter bar. Therefore, attenuation/dispersion of the strain signal with increasing propagation distance down the transmitter bar appears to occur solely in simulations where the specimen exhibits a brittle failure. In mesoscale simulations “IR_HC_0003” and “IR_HC_0005”, which both exhibited a more progressive failure, there is not a noticeable decrease in amplitude of the strain signal as it propagates away from the specimen.

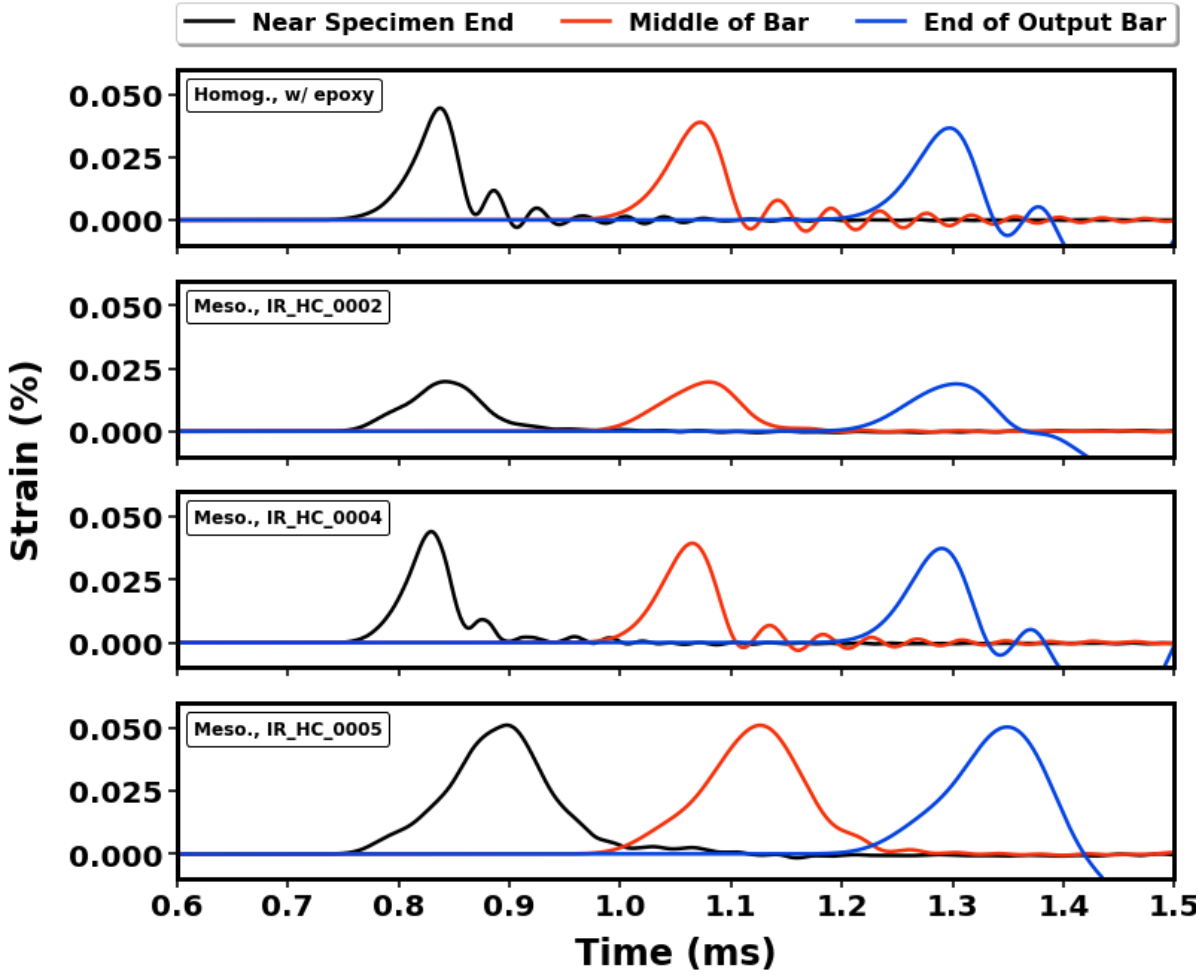

Fig.13: Simulated strain gage signals at various locations along the length of the transmitter bar for the homogeneous mesh case with epoxy and maximum principal failure stress of 280 MPa and mesoscale simulations “IR_HC_0002”, “IR_HC_0004”, and “IR_HC_0005”.

Fig.14 shows the simulated section forces at each end of the of the mesoscale specimen gage section and force at the transmitter bar strain gage in mesoscale simulation “IR_HC_0005” on the same plot as the force on the transmitter bar in the test. The same is shown in Fig.15, but for a version of simulation “IR_HC_0005” with a more refined SHPB mesh (no change to mesoscale specimen mesh) denoted “IR_HC_0005R”. The only difference between a) and b) in these figures is how the simulation data is shifted in time to facilitate comparison with the test data. In Fig.14a and Fig.15a, the simulated specimen forces have all been shifted by the same amount to align the simulated and experimental force at the transmitter bar strain gage. In Fig.14b and Fig.15b, the simulated forces have been shifted to align all three of them with the experimental force at the transmitter bar strain gage. Fig.16 and Fig.17 show the same data as is shown in Fig.14a and Fig.15a with the simulated and experimental incident bar forces also shown.

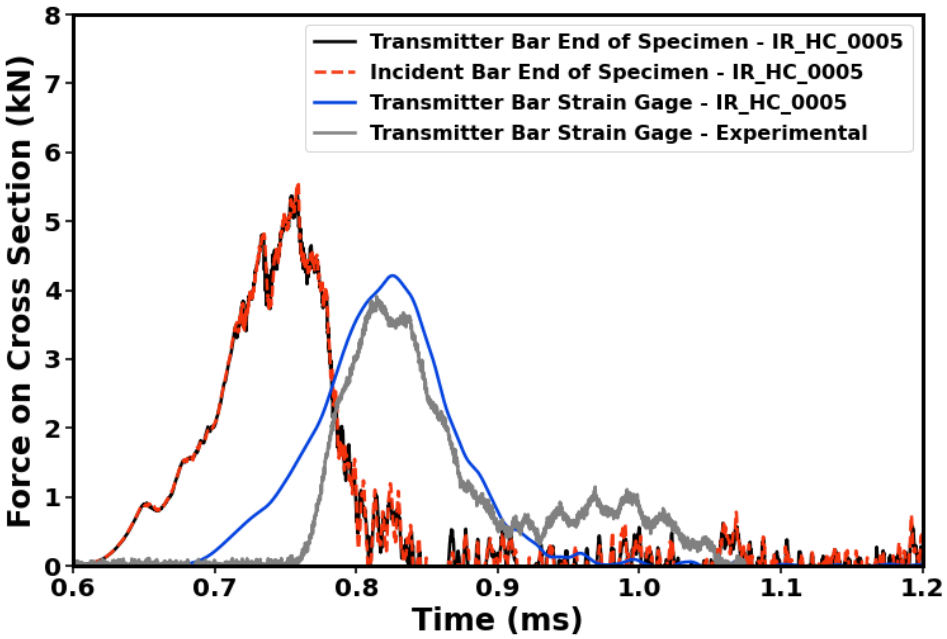

a)

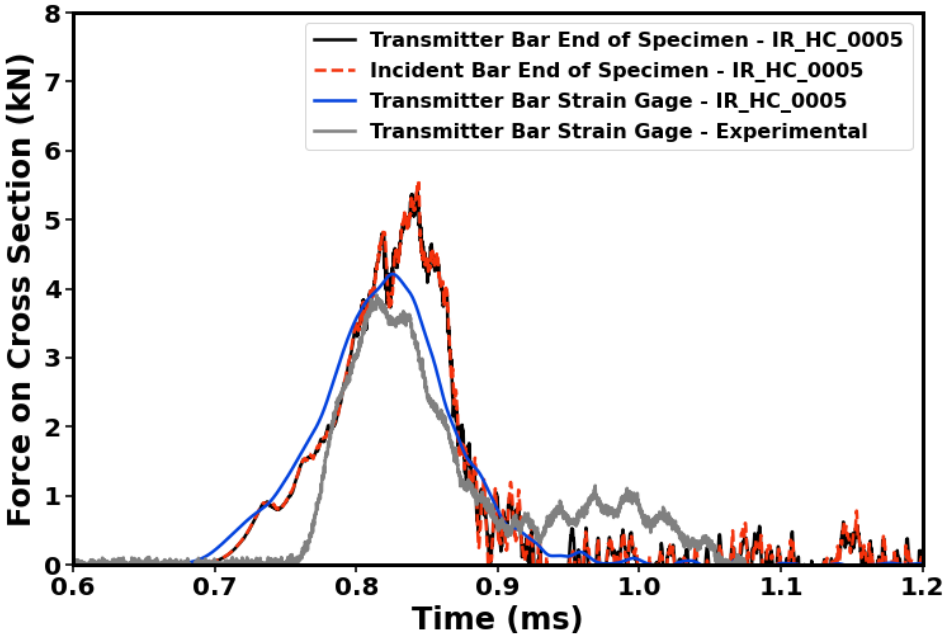

b)

Fig.14: Simulated section forces at each end of the of the mesoscale specimen gage section and force at the transmitter bar strain gage in mesoscale simulation "IR_HC_0005" compared to the force on the transmitter bar in the test. a) simulated specimen forces all shifted by the same amount to align simulated and experimental transmitter bar force. b) simulated forces shifted to align all three of them with the experimental transmitter bar force.

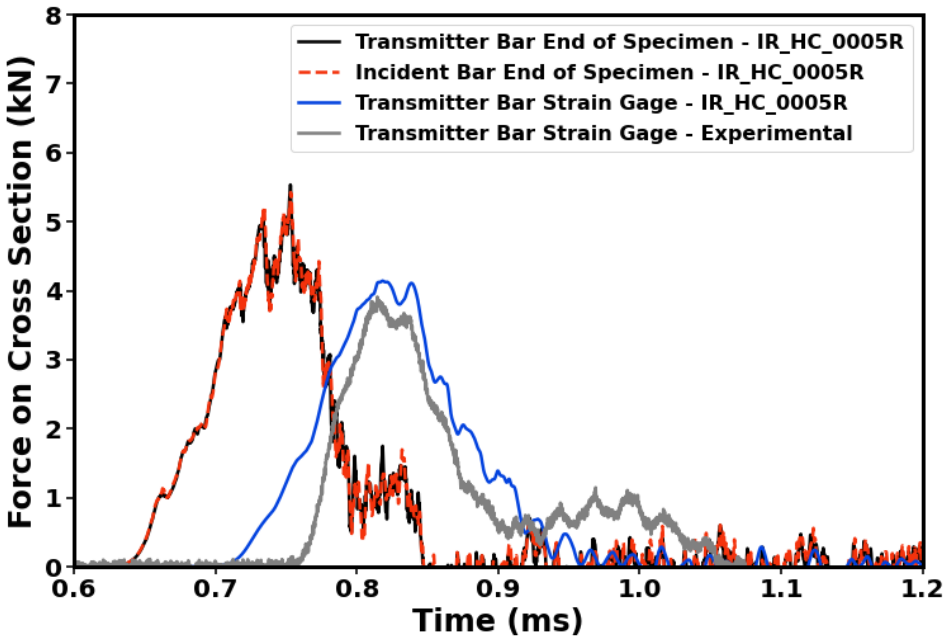

a)

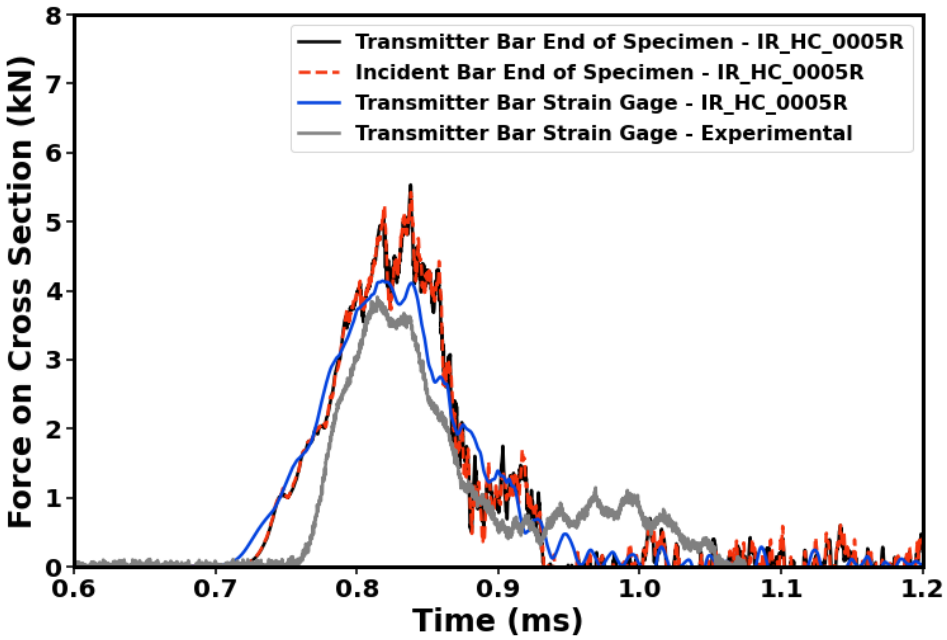

b)

Fig.15: Simulated section forces at each end of the of the mesoscale specimen gage section and force at the transmitter bar strain gage in mesoscale simulation "IR_HC_0005R" compared to the force on the transmitter bar in the test. a) simulated specimen forces all shifted by the same amount to align simulated and experimental transmitter bar force. b) simulated forces shifted to align all three of them with the experimental transmitter bar force

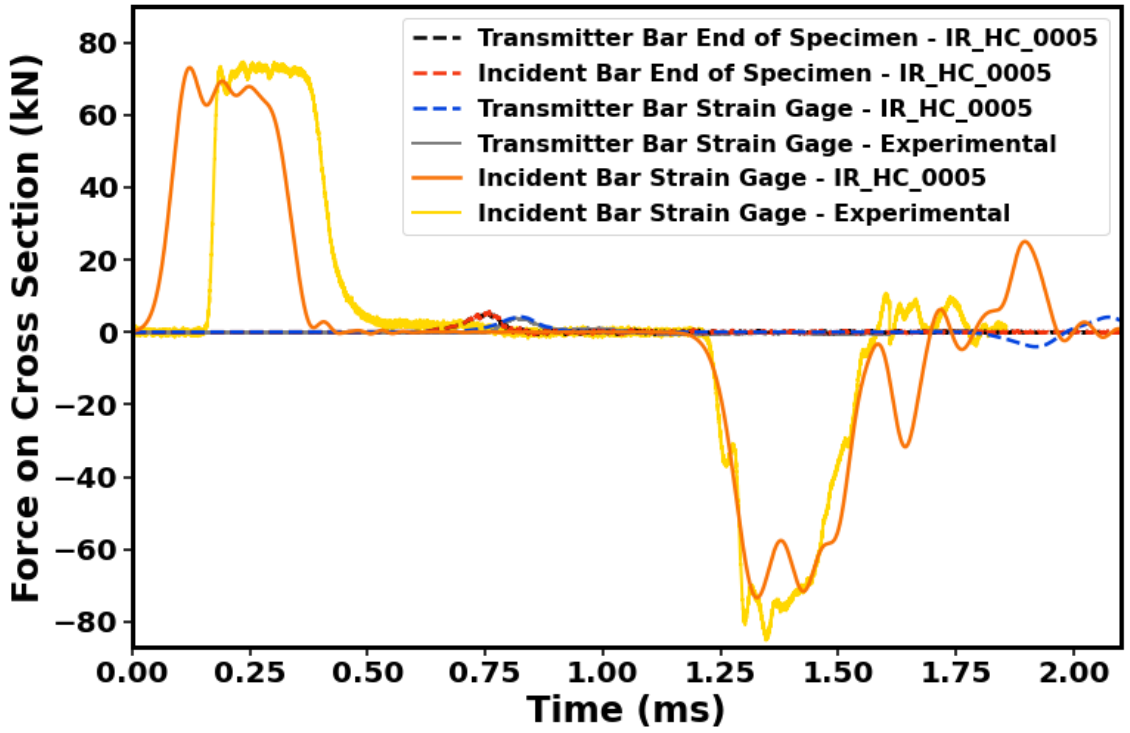

Fig.16: Forces on the incident and transmitter bars in mesoscale simulation "IR_HC_0005" and experiment. Simulated specimen section forces (see Fig.14 for more detail) also shown.

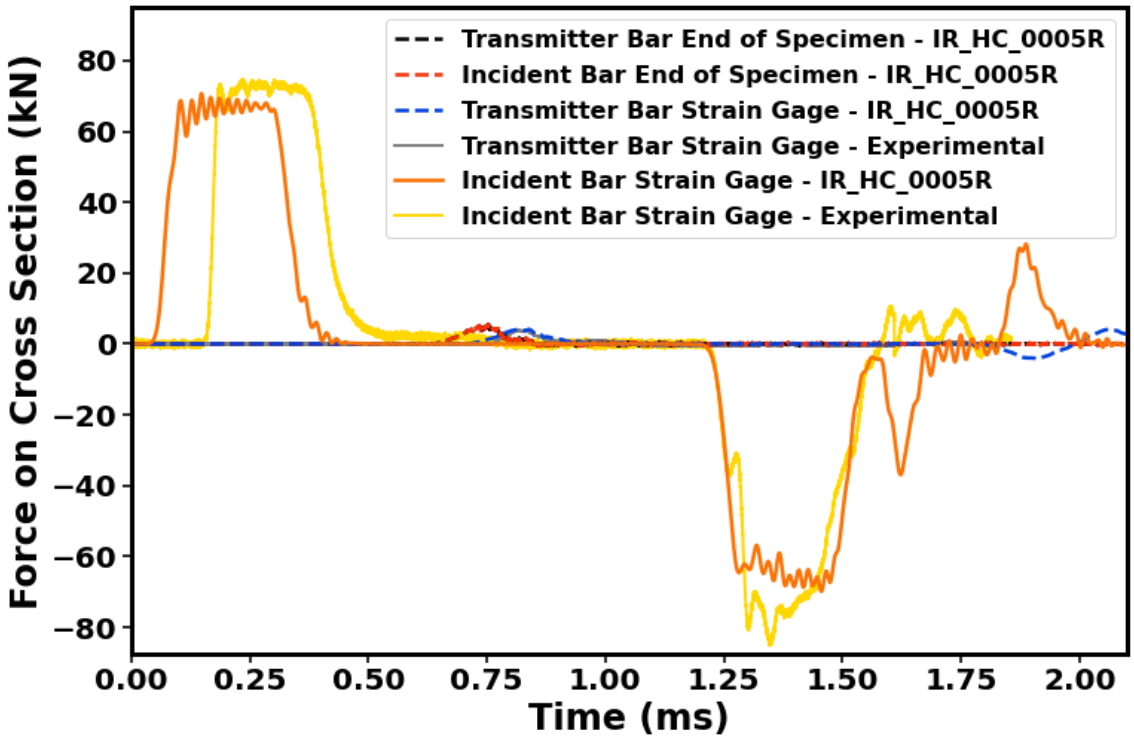

Fig.17: Forces on the incident and transmitter bars in mesoscale simulation "IR_HC_0005R" and experiment. Simulated specimen section forces (see Fig.15 for more detail) also shown.

It is evident that the simulation with the refined mesh (Fig.15) results in a slightly more realistic slope-up of the force vs. time curve and is able to capture the double peak present in the test data. More importantly, the similarity of the simulated specimen section forces and in Fig.14 and Fig.15 indicate equilibrium is achieved during the test. Moreover, the similarity of the simulated specimen section forces with the simulated and experimental force at the transmitter bar gage, and the fact that the transmitter bar signal does not decrease in amplitude as it travels down the bar (Fig.13), indicates the force at the transmitter bar gage in the test is representative of that experienced by the specimen. The incident and reflected wave forces in the simulations and experiment are also in agreement, as shown above in Fig. 16 and Fig.17. It should be noted that the reason there is a slightly larger time difference between the incident and reflected waves in the simulation is likely because the wavespeed of the incident bar in the simulation is slightly lower than that of the actual incident bar. The reason the simulated incident wave occurs earlier in time in time than that of the experiment (Fig.16 and Fig.17) is because, as mentioned earlier, the simulated specimen forces were shifted in time (all by the same amount) to align the simulated and experimental force at the transmitter bar strain gage.

It is interesting and surprising that the the simulation results indicate the test is valid in terms of specimen equilibrium despite the disparity of the forces on the incident and transmitter bar-specimen interfaces computed from the strain gage signals from the test using Equations 1 and 2 (Fig.4, Fig.16, Fig.17), which seem to indicate the opposite. It is currently unclear what exactly happens to the incident wave to result in such a low transmitted force.

Recently, additional SHPB tests were performed on C/C specimens with gage widths ranging from 0.16" through 0.38" and a gage length nominally the same as that of the specimen considered in this manuscript (Fig.1). Different combinations of impact speeds and pulse shapers were used in these tests, the goal of which was to determine which combination of parameters produce the best results. The test data showed that equilibrium was achieved only in tests that used aluminum pulse shapers. Additionally, testing revealed that impacting at speed above 225 in/s resulted in a fracture in the epoxy inside the grips, causing the specimen to slip out of the grip before failure can occur. This phenomenon occurred with two different geometries and did not occur at speeds below 225 in/s with the same geometries. Only specimens with gage widths between 0.25" and 0.34" produced good results. Specimens outside of this range either did not fracture correctly or failed to be in equilibrium according to the test data. It is interesting that in these more recent tests, impacting at speed above 225 in/s resulted in a fracture in the epoxy inside the grips, whereas the tests described in this manuscript all had impact speeds of around 300 in/s and failed in the gage section. Future work includes conducting simulations of these tests to better understand why the aluminum pulse shapers and specimens with wider gage sections result in gage signals that indicate equilibrium.

4 Summary

LS-DYNA simulations of tensile SPHB tests conducted on a C/C CMC were conducted to investigate apparent non-equilibrium suggested by test data and assess the validity of the tests. Simuations with a homogeneous mesh of the test specimen resulted in brittle failure of the specimen and attenuation of the transmitter bar signals with increasing propagation distance down the bar. While simulated section forces in the homogeneous specimen did indicate equilibrium, the simulated transmitter bar signals did not accurately represent the shape of those measured at the transmitter strain gage in the test. Simulations with a mesoscale mesh of the specimen that explicitly represented the tows and matrix resulted in transmitter bar signals that were in better agreement to those measured in the test and that did not become attenuated as they propagated along the transmitter bar away from the specimen. The progressive failure in the mesoscale simulations indicated that the attenuation of the transmitter bar signal observed in the homogeneous simulations was due to the overly brittle failure of the material, which is not representative of the actual failure of the tested C/C specimens. In the mesoscale simulations, specimen section forces also indicated equilibrium was achieved during the tests. The similarity of the simulated mesoscale specimen section forces with the simulated and experimental force at the transmitter bar gage, and the fact that the transmitter bar signal did not decrease in amplitude as it travels down the bar in the mesoscale simulations, indicates the force at the transmitter bar gage in the test is likely representative of that experienced by the specimen. The mesoscale simulations therefore helped in verifying that equilibrium does indeed appear to be achieved in these tests despite the suggestion of the contrary by the test data.

5 Literature

[1] Technical Data Sheet – Woven Carbon-Carbon Composite Grade Properties. CeraMaterials. https://www.ceramaterials.com/wp-content/uploads/2019/12/Woven-CFC-Properties.pdf

[2] Carbon-Carbon Composites. GraphiMaterials. https://www.graphimaterials.com/carbon-carbon-composites.html

[3] Leanos, A. L., & Prabhakar, P. (2016). Computational modeling of carbon/carbon composites under thermal shock conditions. *Composite Structures*, *143*, 103-116.

[4] Hopkinson, B. (1914). X. A method of measuring the pressure produced in the detonation of high, explosives or by the impact of bullets. *Philosophical Transactions of the Royal Society of London. Series A, Containing Papers of a Mathematical or Physical Character*, *213*(497-508), 437-456.

[5] Kolsky, H. (1949). An investigation of the mechanical properties of materials at very high rates of loading. *Proceedings of the physical society. Section B*, *62*(11), 676.

[6] Lindholm, U. S. (1964). Some experiments with the split hopkinson pressure bar∗. *Journal of the Mechanics and Physics of Solids*, *12*(5), 317-335.

[7] #242 Split-Hopkinson Pressure Bar Apparatus. (2006). American Society of Mechanical Engineers (ASME). https://www.asme.org/about-asme/engineering-history/landmarks/242-split-hopkinson-pressure-bar-apparatus

[8] SwRI Split-Hopkinson Pressure Bar Apparatus - An Historic Mechanical Engineering Landmark Designated by The American Society of Mechanical Engineers. (2006, December 1). American Society of Mechanical Engineers (ASME). https://www.asme.org/wwwasmeorg/media/resourcefiles/aboutasme/who%20we%20are/engineering%20history/landmarks/242-split-hopkinson-pressure-bar-apparatus.pdf

[9] Gray III, G. T. (2000). Classic split-Hopkinson pressure bar testing. In *Mechanical testing and evaluation* (pp. 462-476). ASM International.